Astron. Astrophys. 320, 878–892 (1997)

ASTRONOMY AND ASTROPHYSICS

Spectroscopic analysis of early-type stars in young stellar groups

I. Differential analysis of the B1V stars in NGC 2244⋆

M. Vrancken[1], **H. Hensberge**[1], **M. David**[2], **and W. Verschueren**[2,⋆⋆]

[1] Royal Observatory of Belgium, Ringlaan 3, B-1180 Brussel, Belgium
[2] University of Antwerp (RUCA), Astrophysics Research Group, Groenenborgerlaan 171, B-2020 Antwerpen, Belgium

Received 2 July 1996 / Accepted 25 September 1996

Abstract. We explore the potential of analysing fast rotating early-type stars differentially with respect to templates derived from a slowly rotating star of the same spectral type. The analysis is successfully applied to the normal B1V stars in NGC 2244, which have projected rotational velocities ranging from 22 to 260 km s^{-1}. A classical non-LTE analysis of the slow rotator #201 results in chemical abundances similar to those of early B-type stars in the field and in Orion. We argue that a differential analysis of the fast rotators relative to a broadened template derived from #201 can still reveal abundance differences of $\gtrsim$0.2 dex, but no evidence was found for differences in metal composition at this level. A differential analysis of H and He line profiles reveals the need to further explore rotation models. Neither the classical approach to stellar rotation, nor the published models that include the influence of rotation on the star's atmosphere can bring the profiles of the slow rotator into complete agreement with those of the fast rotators. An attempt to extend the analysis to a Be star failed. The Be spectrum is described qualitatively and quantitative measurements are made for the emission in the core of the Balmer lines.

Key words: open clusters and associations: individual: NGC 2244 – stars: early-type, abundances, rotation, Be

1. Introduction

The atmospheres of young stars contain information both about the star itself and about the interstellar medium from which the star is born. Early B-type stars are well suited for a study of the distribution of the different chemical species in individual clusters and also throughout the galactic disk (Gehren et al. 1985) due to their intrinsic brightness and their relatively simple atmospheric structure. A considerable drawback, especially when studying intrinsically small samples, is that only the slowest rotators reveal their abundance patterns in a relatively straightforward manner. In former studies (e.g. Fitzsimmons et al. 1990; Kaufer et al. 1994; Kilian-Montenbrück et al. 1994), only slow rotators were used for the determination of cluster abundances. In order to study the abundance scatter within one cluster, there is a need to develop methods to retrieve information from as many stars as possible, including fast rotators. In this paper, a differential analysis method is proposed and tested on a small sample of stars in the young stellar cluster NGC 2244, covering a large range in rotational broadening (up to 260 km s^{-1}) for a given spectral type. Moreover, one of the stars shows pronounced emission characteristics. NGC 2244 is situated in the Rosette region at a distance of 1.5 kpc from the Sun and 11 kpc from the galactic centre while its age is estimated to be 1–4.10^6 yr (Pérez et al. 1989 and references therein).

After a brief description of the observational material in Sect. 2, we give in Sect. 3 the general characteristics of the stars and the absolute analysis of the slow rotator NGC 2244 – 201. The differential analysis of the faster rotators is given in Sect. 4. The analysis of #201 includes abundance estimates for He, C, N, O, Mg, Al and Si. Finally, the results are evaluated in Sect. 5.

2. Observations and data reduction

The spectra were obtained in 1988 with the CASPEC echelle spectrograph at the 3.6 m telescope of ESO at La Silla, Chile, and cover the range from 3717 to 4703 Å in 21 spectral orders that are well-separated by use of the 51.6 lines/mm echelle grating. They were recorded on ESO's CCD#3 (RCA type, 512 x 320 pixels, 40 e^- read-out noise, 10 e^-/ADU) at about 0.13 Å/pixel and with a gaussian-like PSF of FWHM 0.25 Å. The signal-to-noise ratio computed from photon and read-out noise solely is at least 200 at $\lambda > 3900$ Å and then decreases rapidly to 50 at the shortest wavelengths. The data reduction procedure is in essence the one explained by Verschueren et al. (1997) for their

Send offprint requests to: M. Vrancken, Myriam.Vrancken@oma.be

⋆ Based on observations obtained at the European Southern Observatory (ESO), La Silla, Chile and the Observatoire de Haute-Provence (OHP), St. Michel, France

⋆⋆ Postdoctoral Fellow of the Belgian National Fund for Scientific Research (N.F.W.O.)

Table 1. List of the observed B1V stars in NGC 2244. The star numbers are from Ogura & Ishida (1981); classification, visual magnitude V, Walraven photometric parameters and reddening are from Verschueren (1991). Temperature and gravity are from this work. The listed range given for each of them refers to the extreme values inside the error box defined by [Eq. (2)] and shown in Fig. 1. Differential values of temperatures and gravities are accurate up to respectively 250 K and 0.05 dex. $v \sin i$ values are from this work (A), using a template broadening method (see Sect. 4.1), and from Verschueren (1991) (B), using Collins et al. (1991) rotation models applied to Mg II λ4481. The error estimate does not include the uncertainty due to the assumptions of the method.

number	HD	V_J	[B-U]	[B-L]	$E(B-V)_J$	$v \sin i^A$ km s^{-1}	$v \sin i^B$ km s^{-1}	$T_{\rm eff}$ K	$\log g$
80	259012	9.31	+0.005	+0.004	0.43	260±15	276±28	28 300±1000	4.4±0.1
128	259105	9.42	−0.003	+0.001	0.42	205±10	208±21	26 300±1000	4.3±0.1
201	–	9.74	−0.010	−0.003	0.43	22±1.5	<15	27 300±1000	4.3±0.1
353	–	9.49	−0.016	+0.000	0.50	220:	194±29	–	–

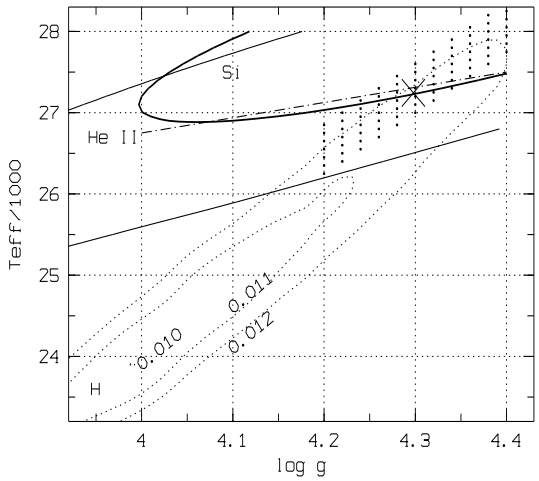

Fig. 1. $T_{\rm eff}$ – log g diagram of #201. The finally adopted parameters are indicated by the cross and the dotted zone indicates the corresponding error box. The (dotted) lines for H correspond to constant levels of χ^2, labelled with the rms of residuals in local intensity as derived from the wings of Hγ, Hδ and Hϵ together. The dashed line indicates where the intensity of the He II λ4686 line is reproduced for a solar abundance. The full lines indicate the zones wherein the χ^2 for the Si equivalent widths [Eq. 1] is low, in the case $v_{\rm turb}$=0 km s^{-1} (thin lines) and $v_{\rm turb}$=4 km s^{-1} (thick line). See Sect. 3.3 for a full explanation.

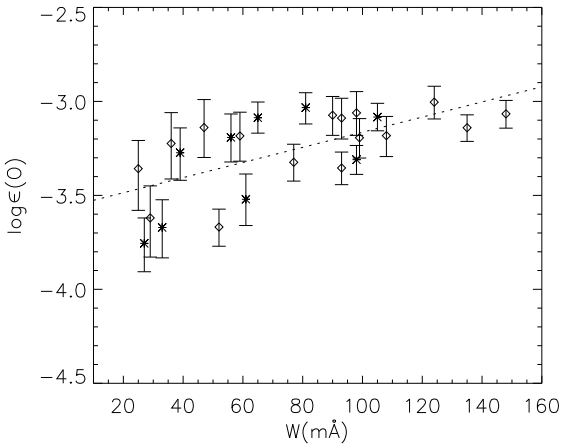

Fig. 2. O abundance versus equivalent width for the unblended O II lines of #201 (for $T_{\rm eff}$=27 300 K, log g=4.3 and $v_{\rm turb}$=0 km s^{-1}). The error bars in the vertical direction are the errors on the abundance induced by uncertainties on the measured equivalent widths. Stars indicate the lines with $\lambda < 4300$ Å while the lines with $\lambda > 4300$ Å are indicated by diamonds. The dashed line is the regression line corresponding to $v_{\rm turb}$=8 km s^{-1}

ECHELEC data, except for some instrument-specific details. For the present purpose, we emphasize that optimal extraction techniques were used and that the wavelength calibration and the determination of a consistent pseudo-continuum received particular attention, because the spectra will be primarily used for radial velocity work (Hensberge et al., 1990). In Sect. 3, we will discuss in more detail the degree of success attained in defining a pseudo-continuum without bias with regard to rotational velocity, as this is a key issue in our analysis.

3. Spectral analysis

3.1. The B1V stars

The stars discussed here (Table 1) were classified as B1V based on low dispersion spectra obtained with the long-slit spectrograph CARELEC at the OHP between 1987 and 1990 (Hensberge & Verschueren 1992; Hensberge et al. 1994). Walraven photometry (Verschueren 1991) confirms that the stars have very similar intrinsic colours. We will refer to these stars through the numbering introduced by Ogura & Ishida (1981).

#201 is a slow rotator, whose numerous metal lines make it suitable for a classical (abundance) analysis based on equivalent width measurements. The other 3 stars are fast rotators whose spectra contain blended metal lines that seldom attain central depths larger than 5%.

#128 was classified by Morgan et al. (1965), and later by Pérez et al. (1987) as B1.5V. Our classification spectrum is more similar to our B1V standard, HD 21 806, than to HD 36 959, our B1.5V standard. The classification spectrum, as well as the intrinsic Walraven colours, suggest that #128 is only marginally cooler than #201.

The papers cited agree on the spectral type of #80 as being B1Vn. Its Walraven colours suggest a marginally cooler tem-

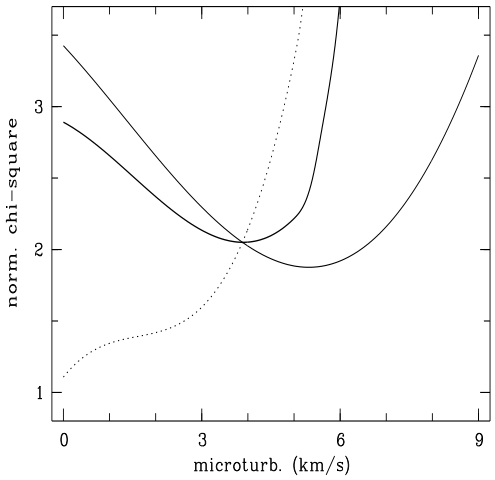

Fig. 3. Normalized values of χ^2 [Eq. (1)] as a function of $v_{\rm turb}$, computed for the Si lines only (dotted line), O lines only (thin full line) and the Si and O lines together (thick full line).

perature than for #128, even after removal of the influence of the 3.5–4 mag fainter #82, at 6.″5 distance. The spectral type B4-A1V of #82 is due to Pérez et al. (1987), who detected strong emission in Hα and weaker emission in Hβ. Analysis of the Hα intensity along the long slit of CARELEC reveals at JD 2 447 217.53 an emission peak in Hα of roughly 50 Å equivalent width, while Hα is in absorption in #80.

#201, #128 and #80 are situated in the central cavity of the Rosette nebula, in contrast to #353. The classification of #353 is somewhat ambiguous, because of the strong emission seen in Hα and in Hβ (at JD 2 447 213.56; emission also seen in low S/N spectra at JD 2 447 567.59), suggesting that also the higher Balmer lines are affected. #353 forms a pair with #354 at 5.″5. #354 is 2.0–2.5 mag fainter; both spectra overlap partly in the long slit of CARELEC. Analysis of the intensity in the cross-order direction confirms that the emission is due to #353. Pérez (priv. comm.) classified the star as B0Ve.

3.2. Atmosphere model and line formation computations

The model atmospheres used are the LTE line-blanketed models of Kurucz (1992) for solar abundances. For a given atmospheric structure, depth dependent non-LTE line formation computations were then performed with the programmes DETAIL and SURFACE (Giddings 1981). The models of the different elements are the following:

- H (Herrero 1987)
- He (Husfeld 1986)
- C II (Eber & Butler 1988)
- N II (Becker & Butler 1989)
- O II (Becker & Butler 1988)
- Mg II (Mihalas 1972; Butler, priv. comm.)
- Al III (Dufton et al. 1986; Becker, priv. comm.)
- Si II, Si III, Si IV (Becker & Butler 1990)

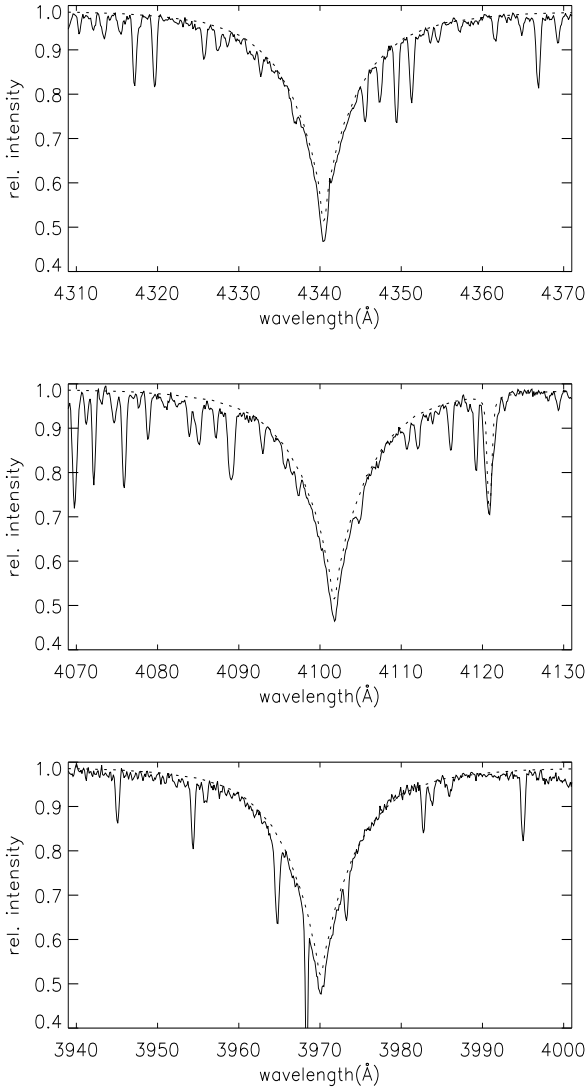

Fig. 4. Fit of Hγ (upper panel), Hδ (middle panel) and Hϵ (lower panel) for $T_{\rm eff}$=27 300 K, log g=4.3. The original data of #201 were multiplied by resp. 0.986, 0.985 and 0.983 in order to remove the mismatch between the empirical pseudo-continuum and the theoretical continuum.

With these model atoms many of the features visible in our spectra can be computed.

In the cited above references it was clearly shown that non-LTE effects are important. All computations made for determining the fundamental atmospheric parameters are performed for a grid of models defined by

- $T_{\rm eff}$: 20 000 – 30 000 in steps of 1000 K
- log g: 4.0 – 4.5 in steps of 0.1 dex
- log ϵ(Si): -5.0 – -4.0 in steps of 0.1 dex (number density relative to total number density on a logarithmic scale)
- $v_{\rm turb}$: 0.0 – 9.0 km s^{-1} in steps of 3.0 km s^{-1}

Table 2. Equivalent widths of the metal lines of #201 which were used for the abundance analysis. In the third column we list observed equivalent widths (W_o), in the fourth column the computed equivalent widths (W_c) for the derived abundances (Table 3), T_{eff}=27 300 K, $\log g$=4.3 and v_{turb}=4 km s^{-1} and in the fifth column the abundances derived from the individual lines for these values of T_{eff}, $\log g$ and v_{turb}. The values between brackets are equivalent widths corresponding to the abundances derived for v_{turb}=0 km s^{-1} (and correspondingly T_{eff}=27 000 K, $\log g$=4.3).

wavelength Å	ion	$W_o \pm \sigma_W$ mÅ	W_c mÅ	$\log \epsilon$
4685.7	He II	75±13	76(66)	-1.05
3920.6	C II	78±6	59(56)	-3.42
4074.8	C II	43±5	50(49)	-3.86
4267.3	C II	132±8	145(143)	-3.98
4374.3	C II	26±5	21(21)	-3.66
4411.5	C II	29±6	38(39)	-3.94
3994.9	N II	83±5	83(76)	-4.43
4035.0	N II	53±6	30(31)	-4.03
4041.2	N II	53±5	44(44)	-4.27
4043.7	N II	21±4	37(38)	-4.80
4176.1	N II	18±4	28(29)	-4.69
4227.7	N II	18±5	14(15)	-4.25
4237.0	N II	39±6	43(45)	-4.49
4241.7	N II	50±7	45(46)	-4.34
4447.0	N II	41±5	44(43)	-4.47
4530.3	N II	27±5	33(35)	-4.56
4607.1	N II	28±5	27(28)	-4.39
4643.0	N II	37±6	34(35)	-4.37
3912.0	O II	105±6	89(88)	-3.23
3945.0	O II	65±5	54(54)	-3.25
3954.4	O II	81±5	71(68)	-3.28
4072.1	O II	98±5	105(99)	-3.51
4078.8	O II	56±7	49(50)	-3.30
4087.2	O II	33±6	50(45)	-3.75
4092.9	O II	39±6	38(35)	-3.39
4185.4	O II	61±7	77(73)	-3.67
4288.7	O II	27±6	53(55)	-3.90

Table 2. (continued)

wavelength Å	ion	$W_o \pm \sigma_W$ mÅ	W_c mÅ	$\log \epsilon$
4303.8	O II	90±9	70(72)	-3.17
4366.8	O II	93±7	84(80)	-3.30
4414.8	O II	135±7	128(120)	-3.35
4443.0	O II	36±8	30(33)	-3.28
4448.3	O II	47±8	37(40)	-3.24
4452.3	O II	59±8	52(53)	-3.31
4590.9	O II	99±7	101(93)	-3.44
4596.1	O II	93±7	100(98)	-3.50
4609.3	O II	52±6	78(79)	-3.77
4641.8	O II	124±7	112(102)	-3.28
4649.1	O II	148±7	141(127)	-3.34
4661.6	O II	98±8	89(83)	-3.31
4676.2	O II	77±6	84(79)	-3.52
4696.3	O II	25±7	26(29)	-3.40
4699.1	O II	108±10	102(98)	-3.34
4701.2	O II	29±8	43(47)	-3.67
4481.2	Mg II	120±8	120(120)	-4.62
4150.0	Al III	36±5	30(32)	-5.72
4479.9	Al III	34±5	47(47)	-6.05
4512.5	Al III	35±5	32(31)	-5.76
4529.0	Al III	53±7	55(53)	-5.85
4128.1	Si II	17±5	0(4)	-4.08
4552.6	Si III	$\lesssim$ 150±6	168(163)	-5.00
4567.8	Si III	134±7	142(139)	-4.89
4574.8	Si III	98±8	91(94)	-4.68
4116.1	Si IV	66±5	57(57)	-4.61
4212.4	Si IV	18±5	12(15)	-4.43
4654.3	Si IV	29±6	22(27)	-4.52

3.3. Absolute analysis of #201

Following Becker & Butler (1990), the principal atmospheric parameters of early B type stars are best constrained by the H-lines and the Si-lines.

Hγ, Hδ and Hϵ are used simultaneously to define a restricted region of interest in the T_{eff} – $\log g$ plane. The use of the higher Balmer lines does not improve the resolution in the T_{eff} – $\log g$ plane because of the lower S/N and the larger difference between the empirical pseudo-continuum level and the theoretical continuum. A least-squares fit to the observed hydrogen profiles (where metal lines were removed) is a compromise between residuals in the far wing, which are due to an incorrect pseudo-continuum level, and between residuals in the line core, which are due to the fact that the theoretical profiles are less deep than the observed lines. Therefore, we treat the continuum of the observed spectrum as an unknown parameter, but with the constraint that only physically plausible values should be accepted. Indeed, the pseudo-continuum derived from data *near* the continuum level probably puts the pseudo-continuum somewhat too low, and this is what the least-squares solutions indicate: the best fit of the line wings requires that the resulting continuum should be $\approx 1.5\%$ above the empirical pseudo-continuum.

The least-squares fits were derived using the gravity-sensitive wings of the observed profiles between the wavelengths where the hydrogen lines have more than 70% residual intensity up to where the theoretical residual intensity reaches 99%. At residual intensities less than 60%, the observed line core is in all cases significantly (as compared to conservative error estimates on the data) deeper than predicted.

The Si lines are then used to narrow down primarily the temperature range compatible with the hydrogen lines. Silicon abundance and microturbulent velocity v_{turb} appear as additional parameters in the problem. In our case, the residuals to the observed equivalent widths increase with v_{turb} (Fig. 3), and even at v_{turb}=0 km s^{-1} the computed Si II and Si IV lines are marginally too weak with respect to the (stronger) Si III lines. This suggests that the conclusion v_{turb}=0 km s^{-1} could possibly be biased by a problem with the Si ionization balance.

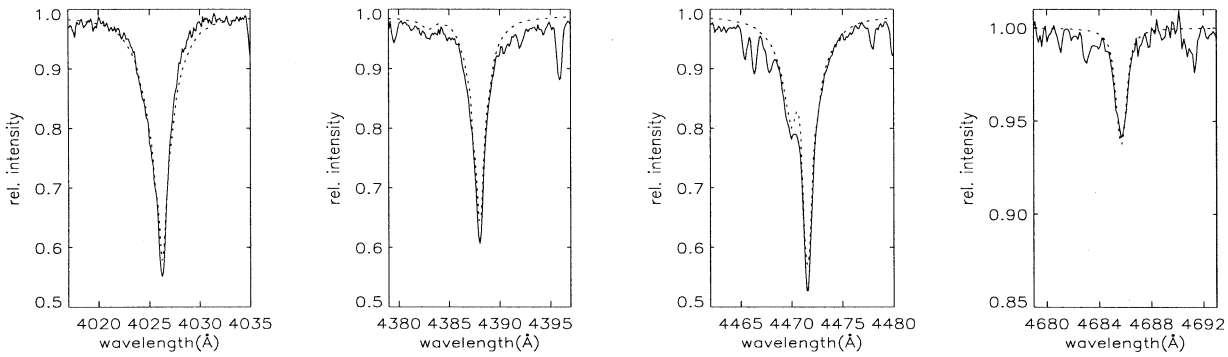

Fig. 5. Fit of the He I lines of #201 at 4026, 4388 and 4471 Å and the He II line at 4686 Å.

A check of $v_{\rm turb}$ can be made using the numerous O II lines. Requiring that they indicate the same abundance irrespective of line strength leads to $v_{\rm turb}$= 8 km s^{-1} when using all O II lines listed in Table 2 (Fig. 2). With such high microturbulence, the equivalent widths of the Si lines cannot be reproduced satisfactorily for any combination of temperature, gravity and abundance. Moreover, for increasing microturbulence, the temperature and gravity indicated by the Si lines become less compatible with those derived from the H lines. We investigated possible causes of bias in the microturbulence value derived from the O II lines:

- A search for unnoticed blends of the stronger O II lines gave no satisfactory explanation.
- Allowing a bias in the determination of the continuum level shortward of Hγ relative to the region longward of Hγ still results in $v_{\rm turb} \simeq$7 km s^{-1} (see Fig. 2).
- A possible bias in the atomic data is suggested by two tests. Firstly, using only multiplet 1, which covers the whole range of equivalent widths, a lower velocity of 5 km s^{-1} is derived. Secondly, there are O II lines whose equivalent width is never reproduced by the models, for any microturbulence in the range 0–9 km s^{-1}. Five lines ($\lambda\lambda$ 3912, 3945, 3954, 4185 and 4609) deviate always more than 2σ and thus cannot contain any valid information on microturbulence. The remaining O II lines also lead to a value of 5 km s^{-1}. Comparison of our equivalent widths with those of other analyses of early B type stars (e.g. Kilian & Nissen 1989) confirms that there is probably a problem with the models, although below 4000 Å the estimation of the continuum level might contribute.

Hence, it appears that uncertainties in atomic data and model assumptions for oxygen and silicon lead to an ill-determined microturbulence, with both species indicating conflicting values when all data and measurement errors are taken at face value. A best estimate of $v_{\rm turb}$, for use in our further analysis, was derived from a χ^2 test on the residuals in equivalent width for all Si (6) and O (20) lines that contain valid information on microturbulence. The model equivalent widths for these tests were computed after deriving optimum temperature, gravity and abundances for every value of $v_{\rm turb}$. Fig. 3 shows that $v_{\rm turb}$=4 km s^{-1} is the best compromise, but depending on the weight given to Si and/or O $v_{\rm turb}$ can lie anywhere between 0 and 5 km s^{-1}.

The assumption $v_{\rm turb}$=4 km s^{-1} leads to $T_{\rm eff}$=27 300 K and log g=4.3 as the best parameters derived from all indicators (H, He, Si, O). Fig. 1 shows the locations of equal sums of residuals in the wings of the three selected hydrogen lines, together with indicators for Si and He II. The curves for H are labelled by the rms average of these residuals. The full lines indicate where for the Si lines

$$\chi^2 = \sum_{\rm lines} \left(\frac{W_{\rm o} - W_{\rm c}}{\sigma_{\rm W}} \right)^2 < 15 \qquad (1)$$

Considering (H, He, Si, O) together, acceptable solutions are located in the zone given by

$$T_{\rm eff} = 27\,300 + 750 \frac{\log g - 4.3}{0.1} \pm 300$$
$$4.2 < \log g < 4.4 \qquad (2)$$

with width 600 K in $T_{\rm eff}$ and with maximum width 0.08 in log g. This error box defines the range wherein the best solution lies, based on all the indicators (H, He, Si, O) but giving them a different relative weight. It thus estimates the uncertainty related to the optimisation *procedure*, but does clearly not include all modeling uncertainties. The hydrogen lines are reproduced better towards its low log g – low $T_{\rm eff}$ boundary, the Si lines better towards higher log g and towards higher $T_{\rm eff}$ if $v_{\rm turb}$ is significantly larger than 0 km s^{-1}. The only observed He II line, near 4686 Å, is less compatible towards the lower gravities in the error box. This incompatibility cannot be avoided through a higher than solar He abundance, since such abundance is in contradiction with the He I lines.

In summary, the temperature, gravity and microturbulent velocity quoted above are the best compromise, further implying log ϵ(Si)=-4.7 and log ϵ(O)=-3.4. The degree of success in predicting H and He lines can be judged from Figs. 4 and 5; the predicted and observed equivalent widths for Si and other metal lines are listed in Table 2.

While the abundances of He, Si and O were fixed simultaneously with $T_{\rm eff}$, log g and $v_{\rm turb}$, the abundances of the other

elements are determined once these fundamental parameters are known. For $T_{\rm eff}$=27 300 K, log g=4.3 and $v_{\rm turb}$=4 km s^{-1}, equivalent widths were computed for 4 abundances: log $\epsilon_{\odot}$-1.0, log $\epsilon_{\odot}$-0.5, log $\epsilon_{\odot}$, log $\epsilon_{\odot}$+0.5, and this for each ion listed in Table 2. The final abundance (see Table 3) is then determined by minimalisation (after interpolation) of χ^2, given by Eq. (1). The equivalent widths (Table 2) were measured by summing the absorption over the line width (with the rotational width as a lower limit), and casually a slightly smaller interval was used to compensate strong line blending in the far wing. Their error estimates include photon (and read-out) noise, and statistical and systematic uncertainties in the continuum placement (similar to Howarth & Phillips 1986).

Abundances vary at most 0.15 dex over the error box in temperature and gravity, with microturbulent velocity fixed. Differences in abundance pattern between #201 and the field stars analysed by Kilian (1992) can be traced back mainly to the somewhat higher average microturbulence assumed in the latter sample. Zero microturbulence would bring the abundances derived from the strongest lines (Mg, Si) to the solar value, but C, N, O and Al abundances would remain on the average a factor two below solar. The lower nitrogen abundance is a direct consequence of smaller measured equivalent widths (compared to measurements of Kilian & Nissen (1989) for stars of the same spectral type), rather than a consequence of line selection or model assumptions.

A non-solar He abundance does not improve significantly the fits of lines of He. Although we eliminated the lines known to be blended or to give problems with the treatment of the broadening mechanisms (Herrero et al. 1992), residuals in different lines (Fig. 5) do not point consistently to a deviating abundance, but probably reflect other model errors. From profile fits of both He I and He II lines, we find that the He abundance does not deviate more than 0.05 dex from the solar He abundance.

Finally, the apparent rotational velocity has been derived by comparing observed and computed FWHM of the O II features listed in Table 2 with $W_{\rm o} > 45$ mÅ. All lines gave consistent values of 22 km s^{-1}, except the λ4448.3 line, which is significantly broader than predicted (leading to $v \sin i$ = 27 km s^{-1}), possibly due to unnoticed blending.

4. Differential analysis

Two different reasons call for a differential analysis when stars produce very similar spectra except for a large difference in projected rotational velocity. Firstly, the differences between the computed lines and the observed ones is often considerably larger than the uncertainties in the observed spectra. Errors in atomic data and simplifying assumptions in atmosphere modelling may both contribute to these discrepancies. The accepted model then results from a compromise between the parameters suggested by different indicators. A slow and a fast rotating star, however, may produce spectra that are, after rotational broadening of the slow rotator, more similar to each other than to the best-fit model. The differential approach exploits fully this similarity. Moreover, such approach is likely to enhance the consistency in the interpretation of small differences in a set of similar stars, since the reference point is precisely defined.

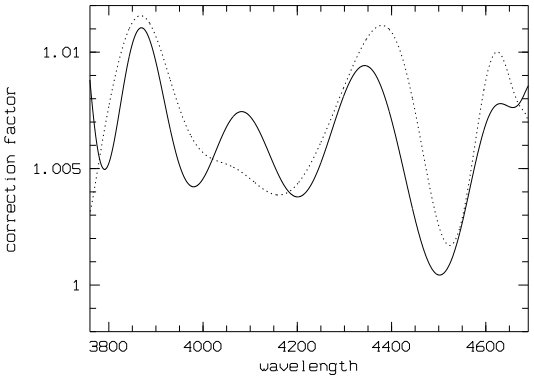

Fig. 6. Correction applied to the empirical pseudo-continuum of the spectrum of #128 (full line) and #80 (dashed line) to make it consistent with the broadened spectrum of #201.

Table 3. Chemical abundances in #201 for $T_{\rm eff}$=27 300 K, log g=4.3 and $v_{\rm turb}$=4 km s^{-1}, compared to solar abundances (Anders & Grevesse 1989), mean abundances of a set of early B-type stars in the field (Kilian et al. 1994) and in the Orion association (Cunha & Lambert 1994). Abundances are expressed as number densities relative to the total number density, on a logarithmic scale. The rms scatter on abundances derived from individual lines is given in column 3, while the abundances derived for $v_{\rm turb}$=0 km s^{-1}, $T_{\rm eff}$=27 000 K and log g=4.3 are given between brackets in the first column. The larger rms for Si is a direct consequence of the choice of $v_{\rm turb}$.

el.	#201	σ	Sun	field stars	Orion
C	-3.80 (-3.80)	0.23	-3.48	-3.78	-3.64
N	-4.42 (-4.38)	0.20	-3.99	-4.22	-4.35
O	-3.41 (-3.28)	0.19	-3.11	-3.48	-3.39
Mg	-4.62 (-4.50)	–	-4.46	-4.62	–
Al	-5.85 (-5.81)	0.15	-5.57	-5.88	–
Si	-4.72 (-4.43)	0.30	-4.49	-4.81	-4.87

Secondly, the basic measurements made on the spectra themselves are liable to bias due to rotational velocity. This is most of all due to the bias on the assumed pseudo-continuum level, but also because of the choice of integration edges and changing contribution of blending lines.

Our method consists of:

- First adressing the consistency of the pseudo-continuum level in the star selected for analysis with respect to the slowly rotating comparison star, assuming that the spectrum of the fast rotator and of the adequately rotationally broadened template are identical at most wavelengths.

- Then changing the atmospheric parameters in such a way that the observed differences between these two spectra are reproduced as differences between the two models. In first instance, gravity and temperature are varied; abundances only

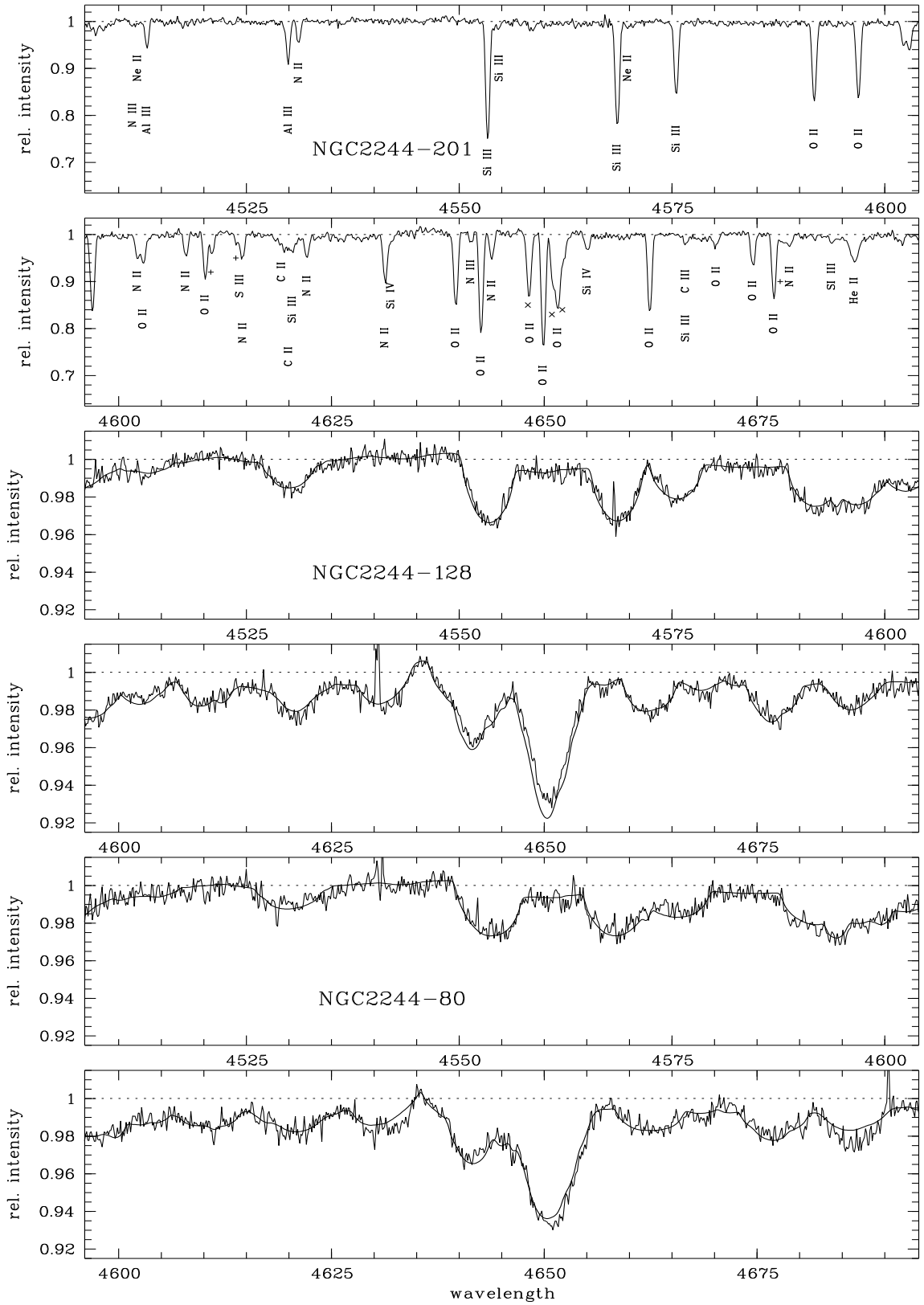

Fig. 7. Spectrum of the sharp lined star #201, of #128 with the corresponding #201 template and of #80 with its #201 template. The identifications are based on those of Kilian et al. (1991). In crowded line regions minor contributions of O II and C III are indicated resp. by '+' and 'x' symbols.

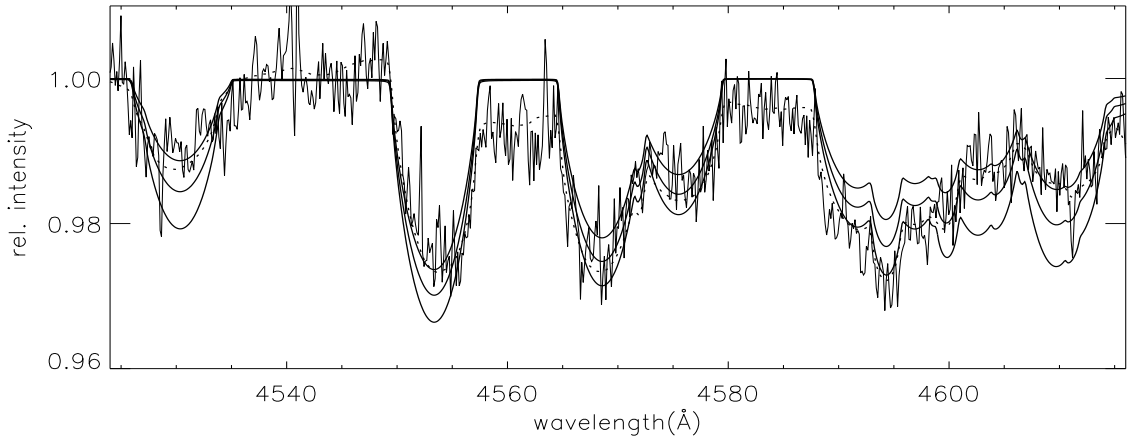

Fig. 8. Selected part of the spectrum of #80, overplotted with the rotationally broadened template #201 (dotted line). Rotationally broadened theoretical spectra for #201 are also shown (thick full lines), for $T_{\rm eff}$=27 300 K, log g=4.3 and $v_{\rm turb}$=4 km s^{-1} and 3 different sets of abundances: all abundances as derived for #201 (see Table 3) and these abundances resp. increased and decreased by 0.2 dex.

Table 4. Residuals of observed spectra relative to the broadened template, for different subsets of data in the range 4505 to 4700 Å. Columns identify: the star (col. 1) ; the number of data points in the considered wavelength range (col. 2); the selected number (col. 3) to calculate the over-all rms (col. 4) avoiding the few outliers; the near-continuum points, i.e. with relative intensity larger than 0.99 in the template (col. 5), selected to calculate an rms estimator less susceptible to differences in the stellar parameters (col. 6); the formal rms expected from photon and read-out noise (col. 7).

star	$n_{\rm inp}$	$n_{\rm all}$	$\sigma_{\rm all}$	$n_{\rm cont}$	$\sigma_{\rm cont}$	$\sigma_{\rm pred}$
80	1514	1510	0.0040	669	0.0037	0.0036
128	1514	1509	0.0035	767	0.0031	0.0031

whenever necessary. Differences in microturbulence are neglected.

4.1. Elimination of spectral differences due to rotation

The spectrum of #201 is assumed to be essentially unbroadened by rotation, and rotationally broadened versions are produced by convolution with the rotation profile (Gray 1976) for the linear limb-darkening law tabulated by Wade & Rucinski (1985). It is not evident a priori that profile variations over the stellar disk can be neglected at the required rotational velocities above 200 km s^{-1} (Collins et al. 1991; Brown & Verschueren 1996), but the excellent agreement with the metal line spectra of the faster rotating stars (Fig. 7) strongly suggests that the simple broadening model is useful for a number of applications. In order to obtain this agreement, we applied a slow-varying correction to the empirical pseudo-continuum level of the faster rotators, as shown in Fig. 6.

The applied correction is reassuringly small, taking into account the obvious dependence on line width of the procedure used for fixing the pseudo-continuum level. Indeed, this level was determined starting from intensities at (rotation-independent) fixed continuum windows, in a procedure that iteratively removes points which are too low from the initial set. The similarity in the wavelength dependence of the correction factors for stars #128 and #80 supports rotation as the dominant cause for the bias. Differences in the wavelength dependence correlate with the position of wide spectral features (H lines and the diffuse interstellar band near 4430 Å), suggesting that the interpolation of the pseudo-continuum in these regions was indeed influenced by the anchor points near these features.

The applied template broadening for each star is expressed in velocity units in Table 1. These values were determined by comparing the broadened spectrum of #201 with the spectrum of the fast rotator in the wavelength region from 4505 to 4700 Å, which is very well suited for this purpose. The corresponding rotational velocities agree within the errors with the values derived by Verschueren (1991) who fitted a more complex rotation model to the stronger Mg II line.

As a by-product, the method provides a useful lower limit to the S/N ratio of the spectra, which can be compared to the formal estimate derived during the data reduction process. One simply assumes that all the spectral differences seen between an observed spectrum and the (broadened) template are the result of noise. The method is most powerful when appropriate spectral intervals, avoiding the lines which are most sensitive to physical differences, are selected. Table 4 summarizes the evidence and shows that the contribution of systematic noise is, in a statistical sense (i.e. for the large majority of data points), negligible relative to the random noise. Such systematic noise could have arisen as a consequence of different sampling over the detector and of inadequate assumptions in the data reduction process. Its most important contribution in the case of differential work, which would obviously dominate over random noise, was thus satisfactorily represented by the low-frequency correction shown in Fig. 6.

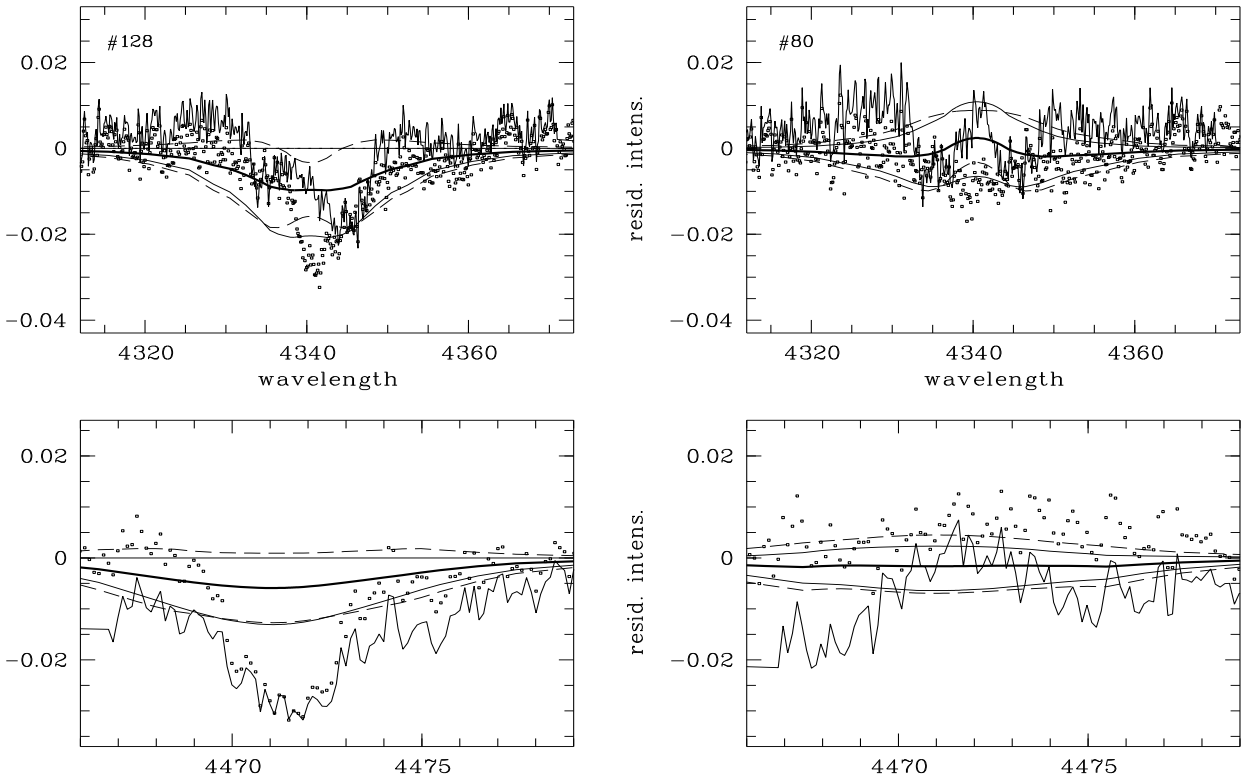

Fig. 9. Residuals in Hγ and He I λ4471 (#128 resp. #80 minus the rotationally broadened template). The dots refer to the classically rotationally broadened template, the thin full line refers to the corrected template for $w_{80} = w_{128} = 0.9$ and $w_{201} = 0.0$ (see Sect. 4.2). For comparison, the thick full line shows the theoretical prediction for the derived atmospheric parameters (Table 1); the smooth thin lines show the effect of a change of 1000 K in the temperature of the fast rotator, while the influence of a change of 0.1 dex in log g is demonstrated by the dashed lines.

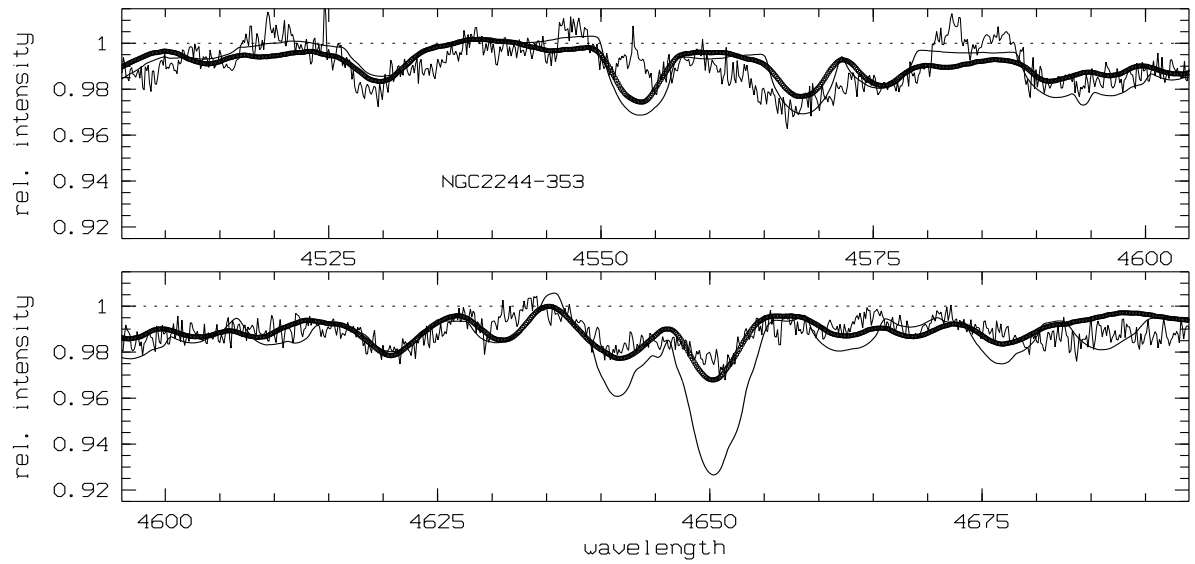

Fig. 10. Spectrum of the Be star #353, compared with #201 as in Fig. 7 and to the B2V star #79 (thick line). Both templates were broadened to 220 km s^{-1}.

4.2. NGC 2244 – 128

All lines sensitive to temperature indicate that #128 is cooler than #201, in accordance with the Walraven photometry, which suggests a difference of 700 K. This conclusion is further corroborated by low-dispersion IUE spectra. The ratio of the extinction-corrected UV flux distributions, $F_{\#201}/F_{\#128}$, can be globally represented as $0.866 - 0.007u - 0.020u^2$ where $u = (\lambda - 2100)/1000$. Comparison with Kurucz (1992) models suggests that #128 is $\simeq$ 1000 K cooler and may have a slightly higher gravity.

The differences in the visual spectra, and in particular the change in the wings of the hydrogen lines and the slightly weaker He II λ4686 suggest $T_{\rm eff}$ $\simeq$26 300 K and $\log g$ $\simeq$4.3. All but the weakest, blended He I lines show very similar changes, in agreement with this lower temperature. However, the changes in the *core* of the hydrogen and helium lines could not be modelled straightforwardly as a differential temperature and/or gravity effect, the main problem being that those changes are restricted to a narrow region around the line centre (both for the H and He lines), while differential temperature, gravity and/or abundance effects predict smoother changes over a larger wavelength range (see Fig. 9). This remains true within the error box for $T_{\rm eff}$ and $\log g$ of the template #201.

In order to explain these discrepancies, we looked into non-classical rotational effects as predicted by Collins et al. (1991) for Hγ and He I λ4471. We corrected the template in these lines by an amount equal to the difference between the line profile computed by Collins et al. for B1V stars at the $v \sin i$ of #128, and the corresponding $v \sin i = 0$ km s^{-1} profile, broadened classically to the same $v \sin i$ (Fig. 9). This wavelength-dependent correction must be calculated for a range of ratios w of angular to (angular) break-up velocity and corresponding angles i. As the available grid in w (0.0, 0.5, 0.8, 0.9, 1.0) and i ($0°, 30°, 45°, 60°, 90°$) is coarse, a suitable interpolation algorithm had to be applied. We assumed that #201 is a truly slow rotator, while for the fast rotators, all possible values of w were considered. Tests with $w_{201} = 0.9$ did not lead to a better agreement with residuals obtained by varying $T_{\rm eff}$ and $\log g$. The correction which was applied to the templates for #128 and #80 was relatively weakly dependent on the value of w.

For #128, this correction to the template deepens the core of Hγ (most at the central 4 Å) and the line wings further outside than 8 Å, which in turn may influence the choice of log g by ≤ 0.15 dex. The violet half of the line is well represented for $w = 0.9$, i.e. $i = 35°$, and the wings now suggest $\log g = 4.2$ rather than 4.3. But due to the asymmetry of the residuals, the red half of Hγ is then not well fitted near the line core. The low $\log g$ is not supported by an analysis of the He I λ4471 line. This line becomes narrower in the corrected template, while its central depth does not change appreciably. It can be reconciled with the observed profile in #128 only when $\log g$ is increased and/or the helium abundance is enhanced. The first possibility is inconsistent with Hγ. The second possibility implies smoother changes over a larger wavelength range, while in addition the maximum effect is predicted at the position of the forbidden line component (near λ4469) and not at the line centre, as observed.

We conclude that some of the effects predicted by Collins et al. (1991) may have been detected in Hγ. In general, however, their predictions for different lines do not point to one consistent set of stellar parameters. Hence, it is not yet possible to improve differential temperature, gravity and abundance estimates by inclusion of their work.

At this rotational velocity, information on abundances relative to the template star #201 is best retrieved from a differential line blocking study in selected wavelength intervals. In the Appendix, we develop first order estimates of the accuracy of differential abundances in fast rotators, in order to evaluate for which ions useful results can be obtained. We used the scatter in the blocking ratios derived for a given ion from different intervals to estimate a differential continuum placement uncertainty $\delta_{\rm c} \approx 0.12\%$. In fact, this empirical estimate of $\delta_{\rm c}$ includes all systematic error sources that act independently on different intervals. While the accuracy on individual intensity points is dominated by random errors (Table 4), the accuracy on differential abundances is dominated by systematic measurement errors (Table 5).

None of the derived abundances differ significantly from the template's. While deviations of *individual* abundances could be detected only with reasonable ($> 2.5\sigma$) significance when $\Delta \log \epsilon > 0.2$ dex, the scatter of the differential abundances derived for different ions (Table 5) is fully consistent with the hypothesis that #128 and #201 have identical abundances. This makes it unlikely that *several* of the studied abundances deviate by more than 0.1 dex from the template's. The only anomalous discrepancy is related to the controversial C II λ4267 line, suggesting that carbon could be a factor 2 overabundant relative to #201. The other C II lines do not support such an overabundance; they are however too strongly blended with oxygen lines to permit a sufficiently reliable abundance determination and hence no quantitative estimate is given for C II.

Table 5. Differential abundances (fast rotator minus #201), as derived from the comparison of line blocking in the indicated (approximate) wavelength ranges. The indicated errors refer to differential continuum uncertainties and random errors (see Appendix), and, between brackets, to random errors only.

el.	λ-range	#80	#128
N	3992–3998	-0.01 ± 0.12 (0.06)	-0.12 ± 0.10 (0.05)
	4234–4247		
O	4067–4081	-0.07 ± 0.08 (0.02)	-0.03 ± 0.08 (0.02)
	4586–4602		
	4638–4682		
Mg	4479–4486	$+0.13 \pm 0.10$ (0.05)	$+0.16 \pm 0.09$ (0.04)
Al	4524–4536	$+0.11 \pm 0.21$ (0.09)	-0.06 ± 0.15 (0.06)
Si	4550–4580	-0.05 ± 0.13 (0.04)	-0.03 ± 0.13 (0.04)

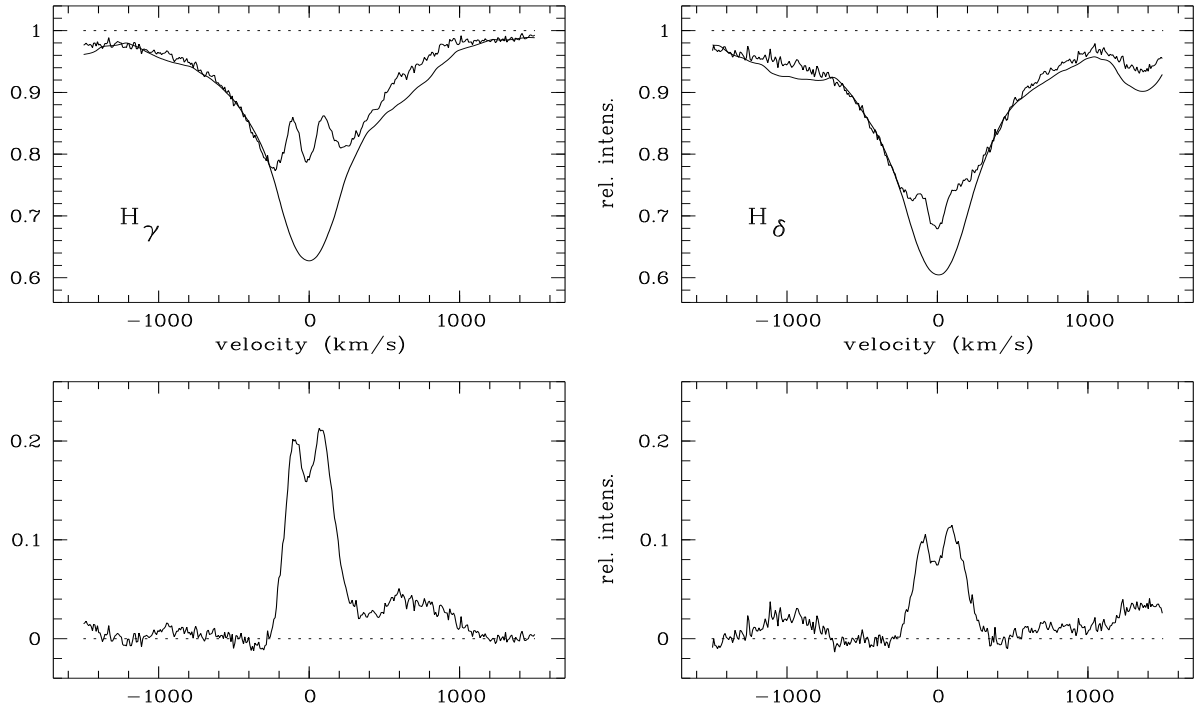

Fig. 11. Emission characteristics of Hγ and Hδ in #353. Upper panels compare the hydrogen lines of the Be star with the #201 template. Lower panels show the pure emission.

4.3. NGC 2244 – 80

#80 resembles #201 more closely and is certainly at least as hot as #201. While both ionization stages of He identify #80 immediately as somewhat hotter, the Balmer lines have, at face value, slightly deeper cores. Almost all He I lines are marginally weaker than in the #201 template, and the He II line is significantly stronger. The high rotational velocity and blending lines in the neighbourhood of the Si IV lines prevent the use of the silicon ionization balance as an additional temperature indicator. The Si II lines are absent. The C III lines make the blended feature near λ4650 (Fig. 7) stronger than in #201. This star is thus certainly not the coolest of the three stars, as indicated by its photometric colours. However, the colour discrepancy is small and in the same sense as predicted by models for rotating stars. Hence, it might well be explainable as due to rapid rotation, but no quantitative estimates for the influence of rotation on the Walraven parameters exist. Neglecting non-classical rotational effects, the most appropriate atmospheric parameters are $T_{\rm eff} \simeq$28 300 K and $\log g \simeq$4.4.

The template corrections due to non-classical rotational effects at 260 km s^{-1} are very similar in shape, but larger than those discussed for #128 (Fig. 9). The core of Hγ and the line wings can be reproduced, with a slightly smaller $\log g$ (=4.3), but the absorption 4 to 8 Å out of the centre is then predicted weaker than observed.

The corrected He I λ4471 line of the template is now so narrow that the preliminary choice of atmospheric parameters for #80 leaves residuals of 1–2 % in the wings. The limitations set by other lines on changes in temperature, gravity and abundance do not allow to explain the major part of these residuals by improving the atmospheric parameters. Hence, the adopted atmospheric parameters, $T_{\rm eff}$=28 300 K and $\log g$=4.4, were selected relying more on the Balmer lines, the depth of the He I lines and the strength of He II λ4686 than on the model-sensitive width of the He I lines.

While the difference of 0.1 in $\log g$ between #128 and #80 is insensitive to the applied rotation model, it is only a question of appreciation of what part of what lines should fit best that determines whether the assumed gravities or 0.1 dex lower gravities relative to #201 are the best values for the fast rotators.

As far as can be judged from the He I profiles of Collins et al. (1991), the line cores are largely independent of the rotational model. The marginally smaller depths of the He I lines can then be interpreted as a differential He underabundance of at most 0.04 dex. Table 5 shows that also in this star any difference in abundance pattern relative to #201 remains below the present level of detectability. Fig. 8 visualizes the spectral changes as a consequence of abundance changes of 0.2 dex at the high rotational velocity of #80.

4.4. NGC 2244 – 353

Emission is clearly visible in the absorption cores of Hγ and Hδ. The metal line spectrum of #353 cannot be matched with a rotationally broadened spectrum of #201 (Fig. 10), while a comparison with the broadened spectrum of the B2V star #79 leads to a better resemblance, but still indicates that the spec-

Table 6. Hδ and Hγ emission line parameters of #353, as derived from the lower panels in Fig. 11. $V_{\rm cd}$, $V_{\rm V}$ and $V_{\rm R}$ are the radial velocities of resp. the the central depression, the violet peak and the red peak, and $I_{\rm cd}$, V and R are the corresponding intensities. W is the emission line equivalent width, FWHM its full width at half maximum. V/R is the violet-to-red peak intensity ratio. $R_{\rm d}$ is the outer emission disk radius, expressed in stellar radii R_*, as determined from the Huang (1972) law. The accuracy estimate reflects mainly the uncertainty on the underlying absorption, except for $R_{\rm d}$ which is most sensitive to $v \sin i$.

	Hδ	Hγ	accuracy
$V_{\rm cd}$ (km s^{-1})	−13	−15	11
$I_{\rm cd}$	0.076	0.163	0.025
$V_{\rm V}$ (km s^{-1})	−93	−95	8
V	0.098	0.201	0.025
$V_{\rm R}$ (km s^{-1})	+ 95	+ 81	8
R	0.110	0.207	0.025
W (Å)	0.51	1.04	0.15
FWHM (km s^{-1})	364	356	10
V/R	0.89	0.97	0.02
$R_{\rm d}$ (R_*)	5.5	6.2	1.6

trum of the Be star does not lend itself to a precise differential analysis relative to a "normal" early B star. The matching of the pseudo-continuum levels of the Be star and a normal star becomes much more subjective and when looking in detail, several metal lines appear distorted. This makes the $v \sin i$ determination particularly troublesome. Therefore we restricted ourselves to a primarily qualitative differential description of the spectrum, which we will give element-by-element. For this purpose, the pseudo-continuum of #353 was corrected ad hoc to that of the templates by assuming a correction identical to the one applied to #128, which has a similar rotational velocity (Fig. 6).

Hydrogen

The Be star #353 shows genuine emission well inside the absorption cores of Hγ and Hδ. The emission line parameters listed in Table 6 describe directly visible characteristics of the pure emission lines (see e.g. Dachs et al. 1992). The pure emission lines (see Fig. 11) were obtained by subtracting the underlying absorption, which we supposed to be equal to the absorption of the rotationally broadened #201. Notice that the apparent "emission" bump near +700 km s^{-1} in Hγ is completely due to the template having much stronger oxygen lines. While the metal line spectrum of the Be star suggests a lower temperature than for #201, comparison with #79 then also suggests a lower $\log g$, so that the H absorption remains similar in #201 and #353. The observation of emission in Hγ and Hδ is not unexpected in view of the earlier detected emission in Hα (W $\simeq$ 30Å) on low dispersion spectra (Verschueren 1991). The cores of the higher Balmer lines up to H8 are weaker than in the corresponding lines of #201, while the core of H9 and the higher Balmer lines are very similar to and even stronger than in #201. While the separation of the two emission components in Hϵ is impossible due to the interstellar Ca II K line, they are definitely not resolved in the higher Balmer lines.

Helium

The strong He I lines have depths comparable to #80, the hottest star in our sample and also the fastest rotator, but He II λ4686 is not visible in #353. Several weak He I lines have intensities similar to those in #128. This pattern can be interpreted as due to red-shifted emission ($\simeq$ 45 km s^{-1}) with a full width of $\simeq$ 350 km s^{-1} in the strongest lines. With #128 as a template, the emission peak intensities are $\simeq$ 0.07 in He I λ3820, λ4026 and λ4471, and decrease to 0.06 in λ4388 and to 0.04 in λ4121 and λ4144. The quantitative estimates of the emission strengths are uncertain insofar as they are extremely dependent on the subtracted template. No emission is seen in He I λ3867, λ3872, λ3927, λ4009, λ4169 and λ4438. Hence, the filling-in by emission appears only in the strongest He I lines and also in He I λ4121.

Carbon

λ4267 is almost as strong as in #79, and definitely stronger than in #128 and the other hotter stars discussed here.

Nitrogen

N II may be weaker than in the comparison stars, but this conclusion is only tentative since the lines are intrinsically faint. The red wing of the line near λ4631 appears to be filled in by emission.

Oxygen

The intrinsic faintness of the O II lines relative to the B1V stars is one of the most striking features in favour of a lower temperature than of #201. The O II lines are marginally weaker than in #79.

Magnesium

λ4481 appears identical to the line in #128, including its width. This led Verschueren (1991) to the conclusion that #353 and #128 have very similar rotational velocities, while the profiles of many other metal lines appear to be more diffuse (Fig. 10). This large diversity in metal line shapes should be better understood in order to be able to give a reliable estimate of $v \sin i$.

Aluminium

The Al III lines are at least as strong as in the other stars of the sample: the λ4529 line has either a disturbed profile or it is blended in a different way than in the other stars.

Silicon

The Si III λ4553/4568/4575 triplet is obviously not reproduced by any of the broadened templates. The λ4553 line is filled in by emission centered at negative velocities (-80 km s^{-1}). Both other lines are more diffuse than the other metal lines – as would be expected for $v \sin i$ = 260 km s^{-1} – and at least as strong in absorption, as could be predicted given the overall spectral characteristics of #353.

From this careful inspection of the spectrum of the Be star, we conclude that its metal line spectrum is more like that of a B2V star than to a B1V star. Furthermore, the Si λ4553 is clearly influenced by the presence of the circumstellar disk, while the effects in other lines are less obvious. The strong He I lines and at least Hγ and Hδ are partly filled in by emission.

5. Discussion and conclusions

We have made a detailed analysis of the visual spectrum of the slowly rotating B1V star #201 and used it as a template for a differential analysis of fast rotating stars of the same spectral type. We conclude that the three stars #80, #128 and #201 have a very similar chemical composition which agrees reasonably with the published average values for early-B type stars. Nitrogen is slightly less abundant. The spectrum of the Be star #353 is in many aspects nearer to a B2V than to the other B1V stars, but shows several distorted line profiles.

We argue that fast rotators should be analysed by comparing the observed differences between a fast rotator and an appropriately broadened template derived from a slow rotator of the same spectral type, with the correspondingly small differences between models for the fast rotator and the template. Given reasonably high signal-to-noise data, the limiting factors lie in systematic uncertainties related to the continuum placement and to the non-classical influences of rotation on line profiles. Non-classical rotational effects such as those predicted by Collins et al. (1991) and possibly additional atmospheric effects on the formation of H and He lines need to be understood in more detail.

The differential analysis, applied to high S/N spectra, opens possibilities for a larger statistical study of the scatter in chemical composition of stars belonging to the same physical group. Earlier, only the few slow rotators were used to measure this scatter. Kilian et al. (1994) and Kilian-Montenbrück et al. (1994) claim a scatter of the order of a factor 2 for several species in NGC 6231 and NGC 6611. However, a negligible scatter is found in these clusters, in Cep OB III and in h + χ Per by Fitzsimmons et al. (1990) and in NGC 1893 by Rolleston et al. (1993). Cunha & Lambert (1994) find no significant variations across the Orion subgroups for C, N and Fe, but find that O and Si abundances correlate with each other and scatter within a factor 3, with the most enriched stars in these species belonging to the youngest subgroups.

Evidently, the method has to be applied to a much larger sample of stars before it can lead to interesting astrophysical conclusions. In a first stage, we plan to apply such analysis to a sample of $\simeq$ 15 normal O9-B3 stars in NGC 2244 observed at La Silla between 1986 and 1994. This larger sample might also allow us to evaluate better the validity of the existing rotational models, and the possibilities for disentangling rotational velocity and inclination of the rotation axis.

Acknowledgements. M.V. acknowledges financial support of her research by the *Belgian Federal Scientific Services (DWTC/SSTC)*; H.H., M.D. and W.V. carried out the research in the framework of the project *Service Centres and Research Networks*, initiated and financed by the *Belgian Federal Scientific Services (DWTC/SSTC)*. We thank W. Hummel for helpful discussions and R. Truax for providing theoretical line profiles of rotating stars in a digital form. R. Blomme is acknowledged for critically reading the manuscript. This research made use of the CCP7 library, Starlink and ESO-MIDAS software.

Appendix: error estimation for differential abundances in fast rotators

A.1. Random and continuum placement errors

In the normalized spectra of the star ($I_{*\mathrm{i}}$) and of the template (I_{ti}), the ratio of the blocking coefficients measured over a selected wavelength interval with length N pixels,

$$\frac{b_*}{b_\mathrm{t}} = \frac{\sum_\mathrm{i}(1-I_{*\mathrm{i}})/N}{\sum_\mathrm{i}(1-I_{\mathrm{ti}})/N} \tag{A1}$$

is susceptible to systematic additive errors η_* and η_t in the continuum placement. The error δ_c on the ratio of blocking coefficients [Eq. (A1)] is straightforwardly calculated as

$$\delta_\mathrm{c} = \frac{\sum_\mathrm{i}(1-I_{*\mathrm{i}})}{\sum_\mathrm{i}(1-I_{\mathrm{ti}})} - \frac{\sum_\mathrm{i}\frac{1-I_{*\mathrm{i}}+\eta_*}{1+\eta_*}}{\sum_\mathrm{i}\frac{1-I_{\mathrm{ti}}+\eta_\mathrm{t}}{1+\eta_\mathrm{t}}} \tag{A2}$$

$$\approx \frac{\left(\frac{b_*}{b_\mathrm{t}}\right)\eta_\mathrm{t}-\eta_*}{b_\mathrm{t}} \equiv \frac{\eta_\mathrm{eff}}{b_\mathrm{t}} \tag{A3}$$

η_eff is essentially the differential error in the continuum placement of template versus fast rotator.

Random errors, characterized by relative errors (inverse signal-to-noise $\rho_{*\mathrm{i}}$ and ρ_{ti}) on the normalized intensities in both spectra, contribute to the variance σ_r^2 on the ratio of the blocking coefficients as

$$\sigma_\mathrm{r}^2 = \left(\frac{b_*}{b_\mathrm{t}}\right)^2\left(\frac{\sigma^2(b_*)}{b_*^2}+\frac{\sigma^2(b_\mathrm{t})}{b_\mathrm{t}^2}\right) \tag{A4}$$

$$= \left(\frac{b_*}{b_\mathrm{t}}\right)^2\left[\sum_\mathrm{i}\frac{(\rho(I_{*\mathrm{i}})I_{*\mathrm{i}})^2}{(Nb_*)^2}+\sum_\mathrm{i}\frac{(\rho(I_{\mathrm{ti}})I_{\mathrm{ti}})^2}{(Nb_\mathrm{t})^2}\right] \tag{A5}$$

For the rotationally broadened lines of interest to us, all I_i are close to 1, and their relative errors are to a good approximation equal over small wavelength ranges in the same spectrum. Hence, introducing characteristic relative errors ρ_* and ρ_t independent of the value of i, we find straightforwardly

$$\sigma_r^2 \approx N^{-1}\frac{1}{b_\mathrm{t}^2}\left[\rho_*^2+\left(\frac{b_*}{b_\mathrm{t}}\right)^2\rho_\mathrm{t}^2\right] \equiv N^{-1}\frac{1}{b_\mathrm{t}^2}\rho_\mathrm{eff}^2 \tag{A6}$$

Comparing the importance of the two error sources, it follows that their ratio depends only weakly on the amount of blocking. In a first approximation,

$$\frac{\sigma_\mathrm{r}}{\delta_\mathrm{c}} \approx \frac{\rho_\mathrm{eff}}{\eta_\mathrm{eff}}\frac{1}{\sqrt{N}} \tag{A7}$$

For the resolution, S/N and rotational velocities of the material used in this paper, $N \gtrsim 50$ even for a single line, $\rho_\mathrm{eff}^{-1} \approx 150$, we see that differential continuum placement errors will dominate over random errors when $\eta_\mathrm{eff} > 10^{-3}$. Thus, efforts done to get consistent continua (see Fig. 6) result obviously in an important gain in accuracy on blocking coefficients.

A.2. Errors on differential abundances

Errors on differential abundances will be considerably larger than those on the ratio of blocking coefficients. Indeed, measurable lines grow slower than linearly with increasing abundance. Moreover, other error sources will contribute: errors in the atmospheric parameters (discussed by Cunha and Lambert (1994) in an analysis of slow rotators), errors in estimating what part of the measured absorption refers to the studied ion, uncertainties on f-values. We will estimate here only the error arising directly from the random and systematic errors in the measurement of the blocking coefficients as discussed above, with the purpose of investigating for which ions we can hope to extract meaningful information on abundance anomalies.

The measured blocking ratio [Eq. (A1)] is by definition related to the blocking ratio $b(\log\epsilon_*,\alpha_*)/b(\log\epsilon_t,\alpha_*)$ for different abundances $\log\epsilon$ and atmospheric parameters α=($T_{\rm eff}$, $\log g$, $v_{\rm turb}$) as

$$\frac{b_*}{b_t} = \frac{b(\log\epsilon_*,\alpha_*)}{b(\log\epsilon_t,\alpha_*)}\,\frac{b(\log\epsilon_t,\alpha_*)}{b(\log\epsilon_t,\alpha_t)} \tag{A8}$$

The second factor at the r.h.s. of Eq. (A8) describes the change of the blocking ratio due to differences in atmospheric parameters between star and template, and is computed theoretically. The measured blocking ratio is corrected by this factor and then the resulting ratio $b(\log\epsilon_*,\alpha_*)/b(\log\epsilon_t,\alpha_*)$ is interpreted (from comparison with model calculations) as due to an abundance difference.

The uncertainty on $\log\left[b(\log\epsilon_*,\alpha_*)/b(\log\epsilon_t,\alpha_*)\right]$, using Eqs. (A2) and (A6), is given by

$$\sigma\left(\log\left[\frac{b(\log\epsilon_*,\alpha_*)}{b(\log\epsilon_t,\alpha_*)}\right]\right) = \frac{\sqrt{\sigma_r^2+\delta_c^2}}{\ln 10(b_*/b_t)} \approx 0.43\sqrt{\sigma_r^2+\delta_c^2} \tag{A9}$$

In order to relate this error estimate to $\sigma(\log\frac{\epsilon_*}{\epsilon_t})$, we derived a relation between $d\log\epsilon$ and $d\log W$. As a representative case, we computed how a small change of the oxygen abundance (0.1 dex) changed the equivalent widths W of the O II lines for the atmospheric parameters relevant to #201. The relation between (small) changes in $\log\epsilon$ and $\log W$ can be represented for $0 < W < 150$ mÅ as

$$\frac{d\log\epsilon}{d\log W} = \frac{1}{a_0+(1-a_0+a_1W)\exp(-a_2W)} \tag{A10}$$

with $a_0 = 0.253$, $a_1 = 0.01$ and $a_2 = 0.039$. The numerical values of these constants obviously apply only to our specific choice of atmospheric parameters. We will assume that we can apply the same relation to lines of other ions in #201 and similar stars, i.e. that all lines follow the same "curve of growth". Hence, for all ions, the computed derivative $d\log\epsilon/d\log W$ is found to be 2 respectively 3 for $W \approx 40$ resp. $W \approx 75$ and increases to 3.85 at $W \approx 150$. The lines that do not follow this relation deviate all in the direction of a greater sensitivity to abundance. In several cases, but not in all cases, the greater sensitivity can be understood as a consequence of the fact that the line strength refers to a blend of fainter lines, each of which is more sensitive to abundance, as described by the relation above.

Eqs. (A9) and (A10) allow one to evaluate the error on differential abundances, using $b \propto W$, but in the case of several contributing lines, W in the r.h.s. of Eq. (A10) refers to a "characteristic" contributing line (e.g. the strongest line), rather than to the total equivalent width over the whole interval. As the relative uncertainty on the blocking ratios dominates the relative uncertainty on the denominator of Eq. (A10) due to uncertainties in W itself, we have to first order

$$\sigma(\log\left(\frac{\epsilon_*}{\epsilon_t}\right)) = \frac{\sigma\left(\left[\frac{b(\log\epsilon_*,\alpha_*)}{b(\log\epsilon_t,\alpha_*)}\right]\right)}{a_0+(1-a_0+a_1W)\exp(-a_2W)} \tag{A11}$$

The uncertainty on the differential abundance from a single line can then be expressed, using the normalized variables

- $(v\sin i)^* = v\sin i(\mathrm{km\,s^{-1}})/200$
- $\lambda^* = \lambda(\text{Å})/4\,500$
- $\eta^*_{\rm eff} = \eta_{\rm eff}/0.001$
- $\rho^*_{\rm eff} = 150\rho_{\rm eff}$
- $N^* = N/45$
- $f^*(W) = 0.04(a_0+(1-a_0+a_1W)W\exp(-a_2W))$

and using the relation between b and W over an interval of length 2 $v\sin i$, i.e. $b = (Wc)/(2\lambda v\sin i)$, as

$$\sigma\left(\log\frac{\epsilon_*}{\epsilon_t}\right) \approx \frac{0.15(v\sin i)^*\lambda^*}{f^*(W)}\sqrt{0.5((\eta^*_{\rm eff})^2+\frac{(\rho^*_{\rm eff})^2}{N^*})} \tag{A12}$$

Hence, accuracies better than 0.1 dex can only be reached when the blocking is measured over several lines. A group of partly overlapping lines is particularly useful towards higher rotational velocities as the resulting blocking factor increases accordingly, which helps more than the gain in N made in the case of non-overlapping lines. For a few ions, like O II, the use of several intervals with uncorrelated continuum misplacements can reduce the source of systematic errors. Eq. (A12) indicates that the accuracy on differential abundances depends critically on the control over continuum misplacement errors, if sufficiently high signal-to-noise was obtained such that random errors do not dominate.

References

Anders E., Grevesse N., 1989, Geochim. et Cosmochim. Acta 53, 197
Becker S.R., Butler K., 1988, A&A 201, 232
Becker S.R., Butler K., 1989, A&A 209, 244
Becker S.R., Butler K., 1990, A&A 235, 326
Brown A.G.A., Verschueren W., 1996, A&A (in press)
Collins II G.W., Truax R.C., Cranmer S.R., 1991, ApJS 77, 541
Cunha K., Lambert L.L., 1994, ApJ 170, 191
Dachs J., Hummel W., Hanuschik R.W., 1992, A&AS 95, 437
Dufton P.L., Brown P.J.F., Lennon D.J., Lynas-Gray A.E., 1986, MNRAS 222, 712
Eber F., Butler K., 1988, A&A 202, 153
Fitzsimmons A., Brown P.J.F., Dufton P.L., Lennon D.J., 1990, A&A 232, 437
Gehren T., Nissen P.E., Kudritzki R.P., Butler K., 1985, in: "Production and Distribution of C,N,O, Elements", ESO Conference and Workshop Proceedings No. 21, eds. Danziger I.J., Matteuci F., Kjaer K.

Giddings J., 1981, Ph. D. Thesis, University of London
Gray D. F., 1976, "The Observation and Analysis of Stellar Photospheres." J. Wiley & Sons
Hensberge H., Van Dessel E., Burger M., et al., 1990, The Messenger 61, 20
Hensberge H., Verschueren W., 1992, in: "Proc. 4th ESO/ST-ECF Data Analysis Workshop", p. 13-19, eds. Grosbøl P., de Ruysscher R.
Hensberge H., Verschueren W., Rogl J., 1994, in: "The MK Process at 50 Years", A.S.P. Conf. Ser. 60, p. 358-364, ed. C. Corbally
Herrero A., 1987, A&A 171, 189
Herrero A., Kudritzki R.P., Vilchez J.M. et al., 1992, A&A 209, 234
Howarth I.D., Phillips A.P., 1986, MNRAS 222, 809
Huang, S.S., 1972, ApJ 171, 549
Husfeld D., 1986, Dissertation Universität München
Kaufer, A., Szeifert, T., Krenzin R., Baschek B., 1994, A&A 289, 740
Kilian J., 1992, A&A 262, 171
Kilian J., Montenbrück O., Nissen P.E., 1991, A&AS 88, 101
Kilian J., Montenbrück O., Nissen P.E., 1994, A&A 284, 437
Kilian-Montenbrück J., Gehren T., Nissen P.E., 1994, A&A 291, 757
Kilian J., Nissen P.E., 1989, A&AS 80, 255
Kurucz R.L., 1992, Rev. Mex. Astrofis. 23, 45, (eds. Lynas-Gray A.E., Mendoza C., Zeipen C.J.)
Mihalas D., 1972, ApJ 177, 115
Morgan W.W., Hiltner W.A., Neff J.S., et al., 1965, ApJ 142, 974
Ogura K., Ishida K., 1981, PASJ 33, 149
Pérez M.R., Thé P.S., Westerlund B.E., 1987, PASP 99, 1050
Pérez M.R., Joner M.D., Thé P.S., Westerlund B.E., 1989, PASP 101, 195
Rolleston W.R.J., Brown P.J.F., Dufton P.L., Fitzsimmons A., 1993, A&A 270, 107
Verschueren W., 1991, Ph. D. Thesis, Free University of Brussels (V.U.B.)
Verschueren W., Brown A.G.A, Hensberge H., et al., 1997, submitted to PASP
Wade R.A., Rucinski S.M., 1985, A&AS 60, 471

This article was processed by the author using Springer-Verlag LaTeX A&A style file *L-AA* version 3.